

Topological Directional Coupler

Yandong Li,^{1,*} Minwoo Jung,² Yang Yu,¹ Yuchen Han,² Baile Zhang,^{3,4} and Gennady Shvets^{1,†}

¹*School of Applied and Engineering Physics, Cornell University, Ithaca, New York, 14853, USA*

²*Department of Physics, Cornell University, Ithaca, New York, 14853, USA*

³*Division of Physics and Applied Physics, School of Physical and Mathematical Sciences, Nanyang Technological University, 21 Nanyang Link, Singapore, 637371, Singapore*

⁴*Centre for Disruptive Photonic Technologies, The Photonics Institute, Nanyang Technological University, 50 Nanyang Avenue, Singapore, 639798, Singapore*

(Dated: June 10, 2024)

Interferometers and beam splitters are fundamental building blocks for photonic neuromorphic and quantum computing machinery. In waveguide-based photonic integrated circuits, beam-splitting is achieved with directional couplers that rely on transition regions where the waveguides are adiabatically bent to suppress back-reflection. We present a novel, compact approach to introducing guided mode coupling. By leveraging multimodal domain walls between microwave topological photonic crystals, we use the photonic-spin-conservation to suppress back-reflection while relaxing the topological protection of the valley degree of freedom to implement tunable beam splitting. Rapid advancements in chip-scale topological photonics suggest that the proposed simultaneous utilization of multiple topological degrees of freedom could benefit the development of novel photonic computing platforms.

Neuromorphic [1] and quantum [2, 3] computing procedures involve a variety of linear algebra operations on a set of N -dimensional unitary matrices $[U(N)]$. Such operations can be carried out using basic photonic devices — phase shifters and beam splitters. Specifically, an arbitrary N dimensional linear operation can be realized with $N(N-1)/2$ Mach-Zehnder interferometers (MZIs) [4–6]. Although it is challenging to perfectly align all the photonic elements with a free-space optical setup when N becomes large, with guided-wave implementations enabled by modern integrated photonics techniques, all elements can be squeezed on a chip, thus motivating the development of large-scale MZI arrays [7–9]. However, key components of MZIs, directional couplers, sacrifice compactness to minimize the photon loss because the coupled waveguides need long (tens of wavelengths) transition regions to prevent unwanted back-reflections [10].

Topological photonics offers new strategies for light manipulation, particularly suppressing back-reflections [11–13]: the immediate result of topological protection is granted by the conservation of the relevant topological index. For example, first-order \mathbb{Z} and \mathbb{Z}_2 indices (e.g., the Chern, spin-Chern, and valley-Chern numbers) guarantee robust propagation of edge states [14–17] at the domain walls between two topologically distinct bulks of photonic crystals (PhCs) with overlapping band gaps. Applications of topological photonics have also been extended to maintaining the robustness of few-photon quantum states [18–21].

Inspired by the semiconductor pioneer H. Kroemer’s famous phrase, “the interface is the device” [22], we aim to design compact directional couplers by utilizing multimodal topological interfaces that support edge modes characterized by more than one topological index [23]. One candidate for the bulk PhC is a spin photonic crystal

(SPC) [15, 24, 25], whose band gaps are characterized by half-integer spin and valley Chern numbers $C_{s,v} = \pm 1/2$, where $s \in \{\uparrow, \downarrow\}$ and $v \in \{\mathbf{K}, \mathbf{K}'\}$ label the spin and valley degrees of freedom (DoFs), respectively. A domain wall between two SPCs with opposite spin Chern numbers supports two chiral topological edge states in each valley. Their propagation direction is locked to the spin DoF and protected from backscattering by the conservation of the spin DoF. On the other hand, the valley DoF depends on the direction of the domain wall: $\mathbf{K}(\mathbf{K}')$ valleys are well-defined at zigzag domain walls, and the two co-propagating edge states (one per valley) are protected against inter-valley scattering [17, 26, 27].

When the protection of the valley DoF is intentionally broken in a controlled manner such that the spin DoF remains conserved, the two co-propagating states can crosstalk without experiencing backscattering. Such intentional breaking of some (but not all) topological DoFs offers an opportunity for creating topological directional couplers (TDCs). Harnessing the topological protection to suppress backscattering can potentially make TDCs smaller than their conventional counterparts because (a) the transition regions [10] between coupled waveguides become unnecessary; (b) The strong modal overlap between the two valley-polarized states reduces the required length of the crosstalking region. In other words, photonic spin conservation enables unidirectional propagation; Valley hybridization causes a significant (non-evanescent) coupling between the two valley-polarized states and enables a short coupling length. In this Letter, we demonstrate that by arranging the domain wall along the armchair direction and engineering its properties, inter-valley scattering is induced [17, 28–30] in a controllable way, which enables a compact, tunable TDC.

We use the microwave SPCs introduced in Ref. [24, 27]

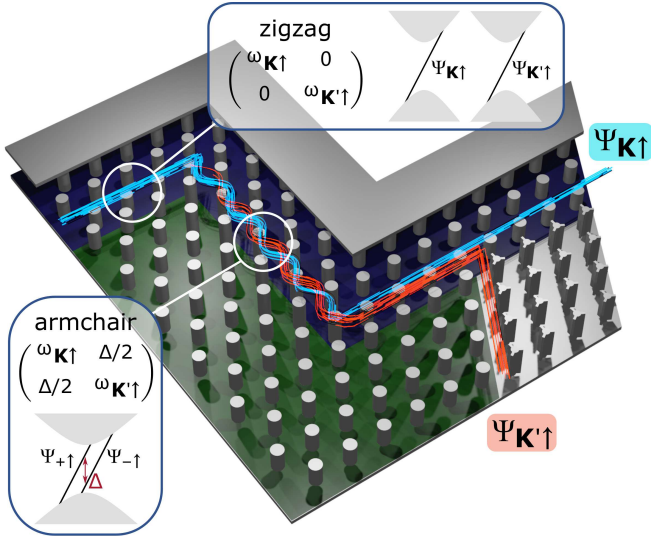


FIG. 1. Topological directional coupler based on a designer domain wall between SPCs. Green (blue) regions: $\text{SPC}^{1(2)}$, metallic rods are attached to the top (bottom) metal plate. The input state $\Psi_{\mathbf{K}\uparrow}$ is injected in a zigzag domain wall, where the valley DoF is conserved. Along the armchair domain wall, the valley basis $\Psi_{\mathbf{K}(\mathbf{K}')\uparrow}$ hybridizes into $\Psi_{+(-)\uparrow}$. The bottom right gray region: VPC for routing valley-polarized modes for detection. Insets: Along the zigzag domain wall, \mathbf{K} and \mathbf{K}' valleys are separated in the k -space, and inter-valley scattering is negligible. The edge-state Hamiltonian is hence diagonal; Along the armchair domain wall, \mathbf{K} and \mathbf{K}' valleys are folded to the Γ point, resulting in a strong inter-valley scattering, and the off-diagonal components in the edge-state Hamiltonian become nonzero.

to implement such a TDC. As depicted in Fig. 1, the structure is based on the domain wall between $\text{SPC}^{1(2)}$, triangular lattices of metallic rods attached to the top (bottom) radiation-confining metallic plates. The photonic spin DoF is synthesized by mixing the TE- and TM-polarized modes, which is accomplished by breaking the reflection symmetry about the mid-height x - y plane [24]. The $\text{SPC}^{1,2}$ possess spin-Chern numbers $C_s^{(1,2)} = \mp 1/2$, accordingly (where the superscript (1) corresponds to $-1/2$ for spin up and $1/2$ for spin down). Details of the physical setup are described in the Supplementary Material. We judiciously arrange the $\text{SPC}^{1,2}$ and let them form a domain wall with a 90° turning corner – the domain wall is zigzag-type before, and armchair-type after the turn (Fig. 1). Along zigzag domain walls, the discrete translational symmetry along one of the primitive lattice vector directions (\mathbf{a}_1 or \mathbf{a}_2) is conserved, and therefore the valley DoF is conserved. In contrast, armchair domain walls are along the $\mathbf{a}_1 + \mathbf{a}_2$ direction, thus changing the discrete translational symmetry and folding both valleys to the Γ point ($k = 0$).

For the zigzag domain wall, the edge-state Hamiltonian is diagonal in the valley basis, $(\Psi_{\mathbf{K}\uparrow}, \Psi_{\mathbf{K}'\uparrow})^T$, because the two valleys are well-separated in the k -space.

When an arbitrary spin-up mode $\Psi_\uparrow = \cos(\theta/2)\Psi_{\mathbf{K}\uparrow} + e^{i\varphi}\sin(\theta/2)\Psi_{\mathbf{K}'\uparrow}$ is guided into or excited in the zigzag domain wall, the proportion of the $\mathbf{K}(\mathbf{K}')$ valley-polarization, which is the modulus squared projection onto the valley-basis, $P_{\mathbf{K}(\mathbf{K}')\uparrow}^{\text{zig}}(l) \equiv |\langle \Psi_\uparrow^{\text{zig}}(l) | \Psi_{\mathbf{K}(\mathbf{K}')\uparrow} \rangle|^2$, is independent of the propagation distance l ,

$$\begin{aligned} P_{\mathbf{K}\uparrow}^{\text{zig}}(l) &= \cos^2 \theta/2, \\ P_{\mathbf{K}'\uparrow}^{\text{zig}}(l) &= \sin^2 \theta/2. \end{aligned} \quad (1)$$

Here, only the spin-up modes are considered because the spin-down ones exit the structure after excitation.

On the other hand, for the armchair domain wall, the edge state Hamiltonian can be represented as $H_{\text{arm}} = (\omega_0, \Delta/2; \Delta/2, \omega_0)$, where $\omega_0 \equiv \omega_{\mathbf{K}\uparrow} = \omega_{\mathbf{K}'\uparrow}$, because the two Dirac cones at the \mathbf{K} and \mathbf{K}' valleys are gapped through the same mechanism. The off-diagonal term $\Delta/2$ represents the \mathbf{K} - \mathbf{K}' inter-valley scattering that hybridizes the valley-polarized modes: The guided mode basis changes from $(\Psi_{\mathbf{K}\uparrow}, \Psi_{\mathbf{K}'\uparrow})^T$ to $(\Psi_{+\uparrow}, \Psi_{-\uparrow})^T$, where $\Psi_{\pm\uparrow} \equiv (\Psi_{\mathbf{K}\uparrow} \pm \Psi_{\mathbf{K}'\uparrow})/\sqrt{2}$. When Ψ_\uparrow enters the armchair domain wall, its time-evolution is governed by the operator $e^{-iH_{\text{arm}}l/v_g}$. Hence, Ψ_\uparrow experiences a Rabi oscillation, and the proportion of the $\mathbf{K}(\mathbf{K}')$ valley polarization, $P_{\mathbf{K}(\mathbf{K}')\uparrow}^{\text{arm}}(l) \equiv |\langle \Psi_\uparrow^{\text{arm}}(l) | \Psi_{\mathbf{K}(\mathbf{K}')\uparrow} \rangle|^2$, becomes

$$\begin{aligned} P_{\mathbf{K}\uparrow}^{\text{arm}}(l) &= \cos^2(\theta/2) \cos^2[\Phi(\Delta)] + \sin^2(\theta/2) \sin^2[\Phi(\Delta)], \\ P_{\mathbf{K}'\uparrow}^{\text{arm}}(l) &= \cos^2(\theta/2) \sin^2[\Phi(\Delta)] + \sin^2(\theta/2) \cos^2[\Phi(\Delta)], \end{aligned} \quad (2)$$

where $\Phi(\Delta) \equiv l\Delta/(2v_g)$. Hence, the armchair domain wall rotates Ψ_\uparrow in the valley basis.

In order to measure the two proportions $P_{\mathbf{K}(\mathbf{K}')\uparrow}(L)$ at the end of the armchair domain wall of length $l = L$, we first restore the valley-DoF-conservation. We let the domain wall make another 90° turn, and the armchair domain wall out-couples to a zigzag one, along which valley-conservation ensures that $P_{\mathbf{K}(\mathbf{K}')\uparrow}(L)$ remains unchanged. Then, we joint a valley photonic crystal (VPC) with the two SPCs to form two single-mode topological waveguides (Fig. 1), and each waveguide supports only one valley-polarization for the spin-up mode [24, 31]. Therefore, the two valley-polarizations are separated, and $P_{\mathbf{K}(\mathbf{K}')\uparrow}(L)$ can be calculated by measuring the output energy of the two single-mode waveguides [25].

To summarize our design, the engineered domain wall performs two changes-of-basis. The guided edge mode basis changes from $(\Psi_{\mathbf{K}\uparrow}, \Psi_{\mathbf{K}'\uparrow})^T$ to $(\Psi_{+\uparrow}, \Psi_{-\uparrow})^T$ and back to $(\Psi_{\mathbf{K}\uparrow}, \Psi_{\mathbf{K}'\uparrow})^T$ again, corresponding to the three different types of domain walls: zigzag SPC^1 - SPC^2 , armchair SPC^1 - SPC^2 , and zigzag $\text{SPC}^{1,2}$ -VPC. This design realizes a unitary transformation, $e^{-iH_{\text{arm}}L/v_g}$, on valley-polarized topological edge modes, $\Psi_{\mathbf{K}(\mathbf{K}')\uparrow}$. The form of this unitary transformation offers two tuning knobs: one is L , the length of the armchair domain wall, which, however, requires significant changes of the structure dimension. The other is the degree of inter-valley scattering,

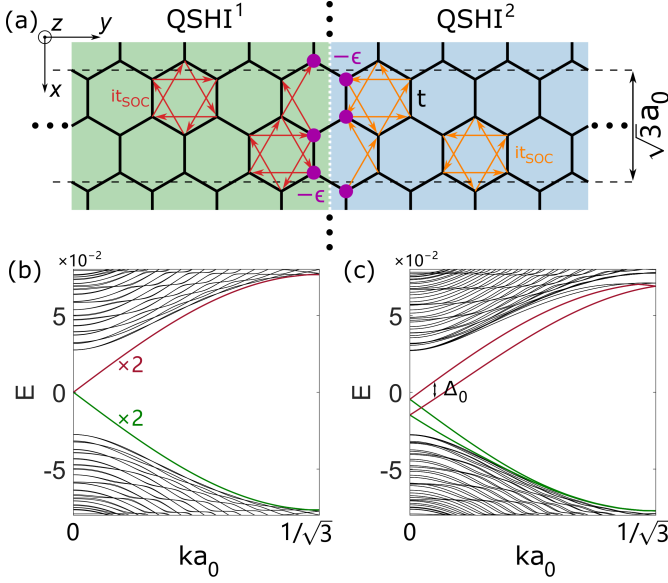


FIG. 2. The tight-binding model. (a) Schematic of the armchair domain wall between two 2D quantum spin Hall insulators (QSHIs). In the green (blue) region, we implement clockwise (counterclockwise) next nearest neighbor (NNN) hoppings [red (orange) arrows] for spin up. For spin down, the NNN hoppings are reversed. The atomic sites adjacent to the domain wall are perturbed with the on-site potential $-\epsilon$ (purple dots). (b,c) Band diagrams of the armchair domain wall with the perturbation (b) $\epsilon = 0$ and (c) $|\epsilon| = 0.42|t|$. In (b), the spin up (down) modes are doubly degenerate. $|t|$ is the nearest neighbor hopping strength.

which is represented by Δ in the off-diagonal entries of H_{arm} and can be tuned by varying unit cell parameters in the vicinity of the domain wall.

The inter-valley scattering amplitude is sensitive to detailed changes along the armchair domain wall. Here, we illustrate the tuning of the \mathbf{K} - \mathbf{K}' -valley hybridization using a tight-binding model. In this model, the quantum spin Hall and quantum valley Hall effects are implemented on a honeycomb lattice with the Kane-Mele model [32] and a staggered on-site potential [33], respectively. All parameters are determined according to the band structure of the corresponding PhCs (see the Supplementary Materials for details). In this idealized model, there is no inter-valley scattering along the unperturbed ($\epsilon = 0$) armchair domain wall, and the spin up (down) edge modes are doubly degenerate. To introduce inter-valley scattering, we perturb the armchair domain wall by applying the on-site potential $-\epsilon$ on the atomic sites along the armchair domain wall. This perturbation hybridizes the valley-polarized modes $\Psi_{\mathbf{K}(\mathbf{K}')\uparrow}$ to $\Psi_{\pm\uparrow}$ (Fig. 2). The energy-splitting between the two hybridized modes, $\Delta \equiv \omega_{+\uparrow} - \omega_{-\uparrow}$, increases linearly with $|\epsilon|$. Specifically, when $|\epsilon| \approx 0.42|t|$, $\Delta = \Delta_0$, where $\Delta_0 \approx 1.1 \times 10^{-2}(2\pi c/a_0)$ (this perturbation is chosen to be consistent with the inter-valley scattering obtained in

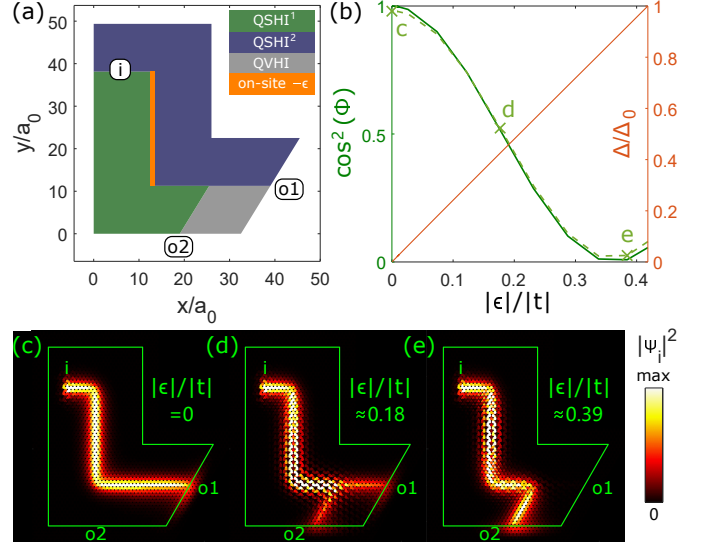


FIG. 3. Tight-binding simulation of the tunable Rabi oscillation. (a) Schematic of the tight-binding model. The green (blue) region represents QSHIs¹⁽²⁾ with clockwise (counterclockwise) next nearest neighbor hopping. The gray region represents the QVHI. The orange line along the armchair domain wall represents the atomic sites that experience the perturbation $-\epsilon$. (b) Analytical (solid line) and tight-binding (dashed line) results of tuning the \mathbf{K} -valley proportion in the output by varying the band-splitting Δ . Δ_0 corresponds to the inter-valley scattering with $|\epsilon| \approx 0.42|t|$ along the armchair domain wall. (c-e) Field profiles of Rabi oscillations with different inter-valley scattering Δ . After exiting the coupling region (armchair domain wall), the state becomes (c) \mathbf{K} -valley polarized, $P_{\mathbf{K}\uparrow}^{\text{TB}} : P_{\mathbf{K}'\uparrow}^{\text{TB}} \approx 1 : 0$; (d) equally \mathbf{K} - and \mathbf{K}' -valley polarized, $P_{\mathbf{K}\uparrow}^{\text{TB}} : P_{\mathbf{K}'\uparrow}^{\text{TB}} \approx 0.5 : 0.5$; (e) \mathbf{K}' -valley polarized, $P_{\mathbf{K}\uparrow}^{\text{TB}} : P_{\mathbf{K}'\uparrow}^{\text{TB}} \approx 0 : 1$.

our experiment when $g = g_0$, Fig. 4) and t is the nearest-neighbor hopping.

The tunable \mathbf{K} - \mathbf{K}' -valley coupling at the armchair domain wall manifests itself when we measure the proportions $P_{\mathbf{K}\uparrow}$ and $P_{\mathbf{K}'\uparrow}$ after the Rabi oscillation. In the tight-binding simulation, we judiciously implemented a source that excites the $\Psi_{\mathbf{K}\uparrow}$ state only. $P_{\mathbf{K}\uparrow}$ and $P_{\mathbf{K}'\uparrow}$ are calculated using the squared amplitude $|\psi|^2$ at the output ports of the two single-mode valley-polarized waveguides, o1 and o2, according to the valley polarization that each waveguide selects: $P_{\mathbf{K}(\mathbf{K}')\uparrow}^{\text{TB}} \equiv \sum_{i \in \text{o1(o2)}} |\psi_i|^2 / \sum_{i \in \{\text{o1}, \text{o2}\}} |\psi_i|^2$. When $|\epsilon| = 0$, inter-valley scattering is completely suppressed ($\Delta = 0$), and the valley DoF is conserved. In this case, almost all the energy is directed to output port o1 and $P_{\mathbf{K}\uparrow}^{\text{TB}} : P_{\mathbf{K}'\uparrow}^{\text{TB}} \approx 1 : 0$, confirming that the output state is \mathbf{K} -valley polarized (Fig. 3c). When $|\epsilon| \approx 0.18|t|$, $\Phi(\Delta) \approx \pi/4$ in Eq. 2, and the output state has equal valley proportions, $P_{\mathbf{K}\uparrow}^{\text{TB}} : P_{\mathbf{K}'\uparrow}^{\text{TB}} \approx 0.5 : 0.5$ (Fig. 3d). Finally, when $|\epsilon| \approx 0.39|t|$, the inter-valley scattering at the armchair domain wall becomes large enough to result in

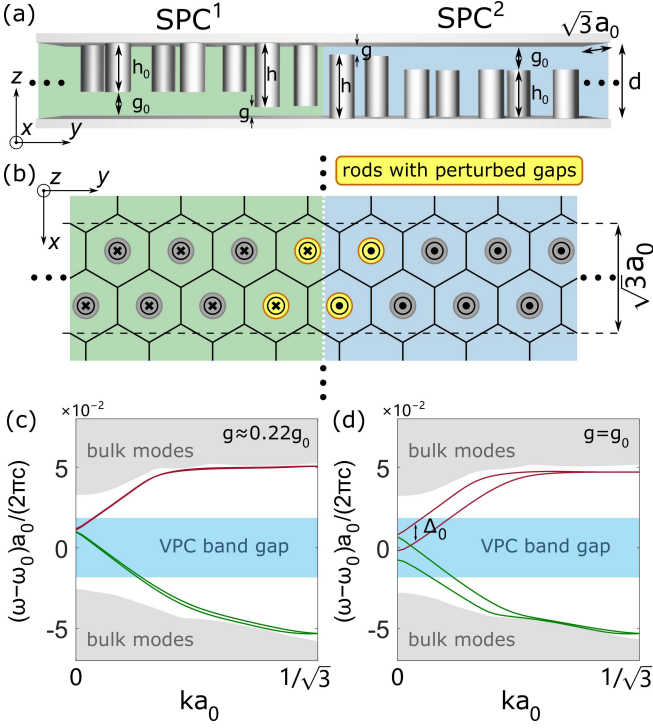


FIG. 4. (a,b) The photonic implementation of the armchair domain wall between QSHI^{1,2} using SPC^{1,2}. The gaps g adjacent to the domain wall are perturbed. (c,d) Photonic edge modes supported by the armchair domain wall with (c) $g \approx 0.22g_0$ and (d) $g = g_0$. Parameters of SPC^{1,2}: $g_0 = 0.15a_0$ is the height of unperturbed gaps; $h_0 = 0.85a_0$, $d = a_0$, where a_0 is the lattice constant. The mid-gap frequency of the VPC band gap is $\omega_0 \approx 0.75(2\pi c/a_0)$.

$\Phi(\Delta) \approx \pi/2$, completely flipping the valley polarization from \mathbf{K} to \mathbf{K}' . Consequently, the output is \mathbf{K}' -valley polarized, $P_{\mathbf{K}\uparrow}^{\text{TB}} : P_{\mathbf{K}'\uparrow}^{\text{TB}} \approx 0 : 1$ (Fig. 3e). The tight-binding model hence confirms that one type of perturbation along the armchair domain wall tunes the inter-valley scattering, and the setup in Fig. 3a can be viewed as a lattice model of a tunable TDC.

To introduce tunability in the photonic implementation of the TDC (Fig. 1), we use the height of the gaps between the rods and the top (bottom) plate and most adjacent to the domain wall, g (Fig. 4a), as the control knob for manipulating the \mathbf{K} - \mathbf{K}' -valley scattering because the electromagnetic field of edge modes is exponentially localized at the domain wall and predominantly concentrated in those gaps. By extending the cavity perturbation theory to incorporate multimodal interactions [34, 35], we find that the effects of perturbing those gaps are mostly confined to each spin subspace – the spin DoF is largely conserved when the valleys are hybridized (see the Supplementary Material for details). When $g \approx 0.22g_0$, the inter-valley scattering is negligible, corresponding to $\Delta \approx 0$ (Fig. 4c). As g increases, the inter-valley scattering is enhanced. When $g = g_0$,

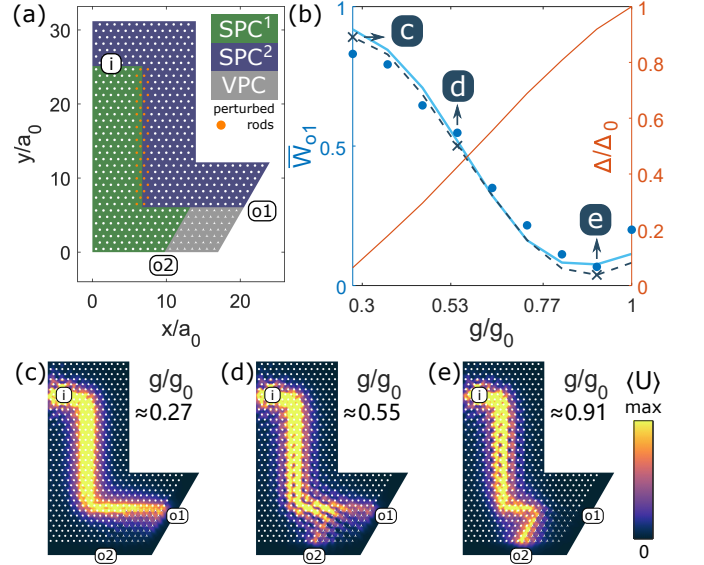


FIG. 5. The experimental implementation and electromagnetic simulation of the TDC. (a) Schematic of the TDC based on topological PhCs. Blue (green) region: SPC² (SPC¹); Gray region: VPC. Orange dots along the armchair domain wall: rods with the perturbed gaps g . (b) Semi-analytical (solid line), simulation (dashed line), and experiment (dots) results of the electromagnetic energy ratio received at output port o1. \overline{W}_{o1} is associated with the \mathbf{K} -valley polarization. Δ_0 corresponds to the inter-valley scattering with $g = g_0$ in Fig. 4a. The experimental data is averaged over the frequency range $\omega_0 < \omega < 1.022\omega_0$, where back-reflection is suppressed (see Supplementary Material for details). (c-e) COMSOL simulation of the beam splitting with three different g values at $\omega \approx 1.01\omega_0$: (c) $W_{o1} : W_{o2} \approx 0.89 : 0.11$; (d) $W_{o1} : W_{o2} \approx 0.50 : 0.50$; (e) $W_{o1} : W_{o2} \approx 0.04 : 0.96$.

the inter-valley scattering at the armchair domain wall causes a strong \mathbf{K} - \mathbf{K}' -valley hybridization with the splitting $\Delta = \Delta_0$ (Fig. 4d) (Note that Δ_0 shares the same value obtained from the tight-binding model with the perturbation setting $|\epsilon| \approx 0.42|t|$.)

The experimental implementation of the TDC was carried out in the microwave regime with $a_0 = 36.8\text{mm}$ (see Fig. 4 for other parameters). We increase the \mathbf{K} - \mathbf{K}' -valley hybridization by incrementing g from $0.27g_0$ to g_0 . We calculate the proportions of the valley polarizations, $P_{\mathbf{K}\uparrow}$ and $P_{\mathbf{K}'\uparrow}$, using the electromagnetic field energy at output ports o1 and o2: $P_{\mathbf{K}(\mathbf{K}')\uparrow}^{\text{exp}} = \overline{W}_{o1(o2)} \equiv W_{o1(o2)} / \sum_{i \in \{1,2\}} W_{oi}$. Experimental results demonstrate that, as the gap height g increases, $P_{\mathbf{K}\uparrow}^{\text{exp}} : P_{\mathbf{K}'\uparrow}^{\text{exp}}$ changes from $0.83 : 0.17$ to $0.07 : 0.93$, agreeing with COMSOL simulations (Fig. 5b-e). In contrast to the tight-binding model, $P_{\mathbf{K}\uparrow} : P_{\mathbf{K}'\uparrow}$ of the photonic structure does not reach $1 : 0$ and $0 : 1$. Two factors give rise to this phenomenon: the imperfectness of the source and the finite dimension of the structure. The excited state is not exactly \mathbf{K} -valley-polarized, instead, the excitation efficiency ratio is $\eta_{\mathbf{K}\uparrow} / \eta_{\mathbf{K}'\uparrow} \approx 43$ for the realistic source.

On the other hand, due to the finite dimension of the VPC, the detection antenna at output port o1 not only receives the transmitted $\Psi_{\mathbf{K}\uparrow}$ but also the evanescent tail of the tunneled $\Psi_{\mathbf{K}'\uparrow}$. Taking both factors into consideration, our semi-analytical model extending Eq. 2 agrees with both simulation and experiment (see the Supplementary Material and Ref. [25] for details).

We have demonstrated a tunable TDC based on tuning the valley-hybridization of edge states via relaxing the topological protection of the valley DoF. With additional delay lines, any arbitrary U(2) operation on the valley-polarized states can be realized using SPC^{1,2} and VPC as elementary building components (see Supplementary Material for details). When the valley-hybridization is tuned, the spin DoF stays conserved for a wide range of frequency (from ω_0 to $1.022\omega_0$, about 50% of the VPC band gap width), and the guided modes remain immune to back-scattering while turning around 90° corners, keeping the structure compact. Moreover, because the edge states supported by the multi-mode waveguiding domain wall originate from the Dirac cones gapped through the same mechanism, they propagate at identical group velocities across the topological band gap, potentially accommodating more complicated light flow manipulations.

Our design offers a new way for developing interferometers – through breaking the protection of one specific topological DoF, the corresponding edge modes are coupled. This paradigm offers a control knob from first principles for adjusting the coupling: the extent of topological-protection-breaking. Therefore, our design is fundamentally different from conventional directional couplers, for which mode hybridization is due to the evanescent coupling of the two waveguide modes and usually tuned by empirically adjusting the waveguide geometry and separation [36]. Additionally, TDCs can scale up with a cascading architecture, similar to MZI meshes. Compared to interferometers based on single-mode topological waveguides [21], our design harnesses the multimodeness and offers controllability via carefully relaxing the valley conservation, both of which could enable applications in microwave metamaterials and quantum computing [37, 38]. With all-dielectric SPCs and VPCs for the telecommunication spectrum [31, 39], the same design can possibly be realized on chip and combined with other topological photonic components [30, 39–42]. Furthermore, with light-controlled index-programmable materials [43–46], the perturbation along the armchair channel could be tuned remotely, paving the way for future progress in integrated photonics, photonic neuromorphic computing, and programmable quantum circuits [47–49].

REFERENCES

-
- * yl2695@cornell.edu
† gshvets@cornell.edu
- [1] Yichen Shen, Nicholas C. Harris, Scott Skirlo, Mihika Prabhu, Tom Baehr-Jones, Michael Hochberg, Xin Sun, Shijie Zhao, Hugo Larochelle, Dirk Englund, and Marin Soljačić. Deep learning with coherent nanophotonic circuits. *Nature Photonics*, 11(7):441–446, Jul 2017.
 - [2] Nicholas C. Harris, Gregory R. Steinbrecher, Mihika Prabhu, Yoav Lahini, Jacob Mower, Darius Bunandar, Changchen Chen, Franco N. C. Wong, Tom Baehr-Jones, Michael Hochberg, Seth Lloyd, and Dirk Englund. Quantum transport simulations in a programmable nanophotonic processor. *Nature Photonics*, 11(7):447–452, Jul 2017.
 - [3] J. M. Arrazola, V. Bergholm, K. Brádler, T. R. Bromley, M. J. Collins, I. Dhand, A. Fumagalli, T. Gerrits, A. Goussev, L. G. Helt, J. Hundal, T. Isacsson, R. B. Israel, J. Izaac, S. Jahangiri, R. Janik, N. Killoran, S. P. Kumar, J. Lavoie, A. E. Lita, D. H. Mahler, M. Menotti, B. Morrison, S. W. Nam, L. Neuhaus, H. Y. Qi, N. Quesada, A. Repeatingon, K. K. Sabapathy, M. Schuld, D. Su, J. Swinerton, A. Száva, K. Tan, P. Tan, V. D. Vaidya, Z. Vernon, Z. Zabaneh, and Y. Zhang. Quantum circuits with many photons on a programmable nanophotonic chip. *Nature*, 591(7848):54–60, Mar 2021.
 - [4] Michael Reck, Anton Zeilinger, Herbert J. Bernstein, and Philip Bertani. Experimental realization of any discrete unitary operator. *Phys. Rev. Lett.*, 73:58–61, Jul 1994.
 - [5] Pieter Kok, W. J. Munro, Kae Nemoto, T. C. Ralph, Jonathan P. Dowling, and G. J. Milburn. Linear optical quantum computing with photonic qubits. *Rev. Mod. Phys.*, 79:135–174, Jan 2007.
 - [6] William R. Clements, Peter C. Humphreys, Benjamin J. Metcalf, W. Steven Kolthammer, and Ian A. Walmsley. Optimal design for universal multiport interferometers. *Optica*, 3(12):1460–1465, Dec 2016.
 - [7] Jacques Carolan, Christopher Harrold, Chris Sparrow, Enrique Martín-López, Nicholas J. Russell, Joshua W. Silverstone, Peter J. Shadbolt, Nobuyuki Matsuda, Manabu Oguma, Mikitaka Itoh, Graham D. Marshall, Mark G. Thompson, Jonathan C. F. Matthews, Toshikazu Hashimoto, Jeremy L. O’Brien, and Anthony Laing. Universal linear optics. *Science*, 349(6249):711–716, 2015.
 - [8] Je-Hyung Kim, Shahriar Aghaeimeibodi, Jacques Carolan, Dirk Englund, and Edo Waks. Hybrid integration methods for on-chip quantum photonics. *Optica*, 7(4):291–308, Apr 2020.
 - [9] Wim Bogaerts, Daniel Pérez, José Capmany, David A. B. Miller, Joyce Poon, Dirk Englund, Francesco Morichetti, and Andrea Melloni. Programmable photonic circuits. *Nature*, 586(7828):207–216, Oct 2020.
 - [10] Menno Poot, Carsten Schuck, Xiao song Ma, Xiang Guo, and Hong X. Tang. Design and characterization of integrated components for sin photonic quantum circuits. *Opt. Express*, 24(7):6843–6860, Apr 2016.
 - [11] Ling Lu, John D. Joannopoulos, and Marin Soljačić.

- Topological photonics. *Nature Photonics*, 8(11):821–829, Nov 2014.
- [12] Alexander B. Khanikaev and Gennady Shvets. Two-dimensional topological photonics. *Nature Photonics*, 11(12):763–773, Dec 2017.
- [13] Tomoki Ozawa, Hannah M. Price, Alberto Amo, Nathan Goldman, Mohammad Hafezi, Ling Lu, Mikael C. Rechtsman, David Schuster, Jonathan Simon, Oded Zilberberg, and Iacopo Carusotto. Topological photonics. *Rev. Mod. Phys.*, 91:015006, Mar 2019.
- [14] Zheng Wang, Yidong Chong, J. D. Joannopoulos, and Marin Soljačić. Observation of unidirectional backscattering-immune topological electromagnetic states. *Nature*, 461(7265):772–775, Oct 2009.
- [15] Alexander B. Khanikaev, S. Hossein Mousavi, Wang-Kong Tse, Mehdi Kargarian, Allan H. MacDonald, and Gennady Shvets. Photonic topological insulators. *Nature Materials*, 12(3):233–239, Mar 2013.
- [16] Konstantin Y. Bliokh, Daria Smirnova, and Franco Nori. Quantum spin hall effect of light. *Science*, 348(6242):1448–1451, 2015.
- [17] Jiho Noh, Sheng Huang, Kevin P. Chen, and Mikael C. Rechtsman. Observation of photonic topological valley hall edge states. *Phys. Rev. Lett.*, 120:063902, Feb 2018.
- [18] Andrea Blanco-Redondo, Bryn Bell, Dikla Oren, Benjamin J. Eggleton, and Mordechai Segev. Topological protection of biphoton states. *Science*, 362(6414):568–571, 2018.
- [19] Michelle Wang, Cooper Doyle, Bryn Bell, Matthew J. Collins, Eric Magi, Benjamin J. Eggleton, Mordechai Segev, and Andrea Blanco-Redondo. Topologically protected entangled photonic states. *Nanophotonics*, 8(8):1327–1335, 2019.
- [20] Sunil Mittal, Elizabeth A. Goldschmidt, and Mohammad Hafezi. A topological source of quantum light. *Nature*, 561(7724):502–506, Sep 2018.
- [21] Yang Chen, Xin-Tao He, Yu-Jie Cheng, Hao-Yang Qiu, Lan-Tian Feng, Ming Zhang, Dao-Xin Dai, Guang-Can Guo, Jian-Wen Dong, and Xi-Feng Ren. Topologically protected valley-dependent quantum photonic circuits. *Phys. Rev. Lett.*, 126:230503, Jun 2021.
- [22] Herbert Kroemer. Nobel lecture: Quasielectric fields and band offsets: teaching electrons new tricks. *Rev. Mod. Phys.*, 73:783–793, Oct 2001.
- [23] Motohiko Ezawa. Topological kirchhoff law and bulk-edge correspondence for valley chern and spin-valley chern numbers. *Phys. Rev. B*, 88:161406, Oct 2013.
- [24] Tzuhsuan Ma and Gennady Shvets. Scattering-free edge states between heterogeneous photonic topological insulators. *Phys. Rev. B*, 95:165102, Apr 2017.
- [25] Yandong Li, Yang Yu, Kueifu Lai, Yuchen Han, Fei Gao, Baile Zhang, and Gennady Shvets. Mode-selective single-dipole excitation and controlled routing of guided waves in a multi-mode topological waveguide. *Applied Physics Letters*, 120(22):221702, 2022.
- [26] Tzuhsuan Ma and Gennady Shvets. All-si valley-hall photonic topological insulator. *New Journal of Physics*, 18(2):025012, feb 2016.
- [27] Fei Gao, Haoran Xue, Zhaoju Yang, Kueifu Lai, Yang Yu, Xiao Lin, Yidong Chong, Gennady Shvets, and Baile Zhang. Topologically protected refraction of robust kink states in valley photonic crystals. *Nature Physics*, 14(2):140–144, Feb 2018.
- [28] Kyoko Nakada, Mitsutaka Fujita, Gene Dresselhaus, and Mildred S. Dresselhaus. Edge state in graphene ribbons: Nanometer size effect and edge shape dependence. *Phys. Rev. B*, 54:17954–17961, Dec 1996.
- [29] L. Brey and H. A. Fertig. Electronic states of graphene nanoribbons studied with the dirac equation. *Phys. Rev. B*, 73:235411, Jun 2006.
- [30] Yandong Li, Yang Yu, Fengyu Liu, Baile Zhang, and Gennady Shvets. Topology-controlled photonic cavity based on the near-conservation of the valley degree of freedom. *Phys. Rev. Lett.*, 125:213902, Nov 2020.
- [31] Yuhao Kang, Xiang Ni, Xiaojun Cheng, Alexander B. Khanikaev, and Azriel Z. Genack. Pseudo-spin–valley coupled edge states in a photonic topological insulator. *Nature Communications*, 9(1):3029, Aug 2018.
- [32] C. L. Kane and E. J. Mele. Quantum spin hall effect in graphene. *Phys. Rev. Lett.*, 95:226801, Nov 2005.
- [33] Gordon W. Semenoff. Condensed-matter simulation of a three-dimensional anomaly. *Phys. Rev. Lett.*, 53:2449–2452, Dec 1984.
- [34] J. C. Slater. Microwave electronics. *Rev. Mod. Phys.*, 18:441–512, Oct 1946.
- [35] George E. Dombrowski. Matrix formulation of Slater’s cavity perturbation theorem. *Journal of Applied Physics*, 55(7):2648–2650, 04 1984.
- [36] Andrea Crespi, Roberto Osellame, Roberta Ramponi, Daniel J. Brod, Ernesto F. Galvão, Nicolò Spagnolo, Chiara Vitelli, Enrico Maiorino, Paolo Mataloni, and Fabio Sciarrino. Integrated multimode interferometers with arbitrary designs for photonic boson sampling. *Nature Photonics*, 7(7):545–549, Jul 2013.
- [37] Lianlin Li, Hanting Zhao, Che Liu, Long Li, and Tie Jun Cui. Intelligent metasurfaces: control, communication and computing. *eLight*, 2(1):7, May 2022.
- [38] Xiu Gu, Anton Frisk Kockum, Adam Miranowicz, Yu xi Liu, and Franco Nori. Microwave photonics with superconducting quantum circuits. *Physics Reports*, 718-719:1–102, 2017. Microwave photonics with superconducting quantum circuits.
- [39] Mikhail I. Shalaev, Wiktor Walasik, Alexander Tsukernik, Yun Xu, and Natalia M. Litchinitser. Robust topologically protected transport in photonic crystals at telecommunication wavelengths. *Nature Nanotechnology*, 14(1):31–34, Jan 2019.
- [40] Tianwei Wu, Yankun Li, Xilin Feng, Shuang Wu, Zihe Gao, and Liang Feng. Topological photonic lattice for uniform beam splitting, robust routing, and sensitive far-field steering. *Nano Letters*, 23(9):3866–3871, 2023. PMID: 37093959.
- [41] Sabyasachi Barik, Aziz Karasahin, Sunil Mittal, Edo Waks, and Mohammad Hafezi. Chiral quantum optics using a topological resonator. *Phys. Rev. B*, 101:205303, May 2020.
- [42] Yongquan Zeng, Udvash Chattopadhyay, Bofeng Zhu, Bo Qiang, Jinghao Li, Yuhao Jin, Lianhe Li, Alexander Giles Davies, Edmund Harold Linfield, Baile Zhang, Yidong Chong, and Qi Jie Wang. Electrically pumped topological laser with valley edge modes. *Nature*, 578(7794):246–250, Feb 2020.
- [43] Han Zhao, Xingdu Qiao, Tianwei Wu, Bikashkali Midya, Stefano Longhi, and Liang Feng. Non-hermitian topological light steering. *Science*, 365(6458):1163–1166, 2019.
- [44] Tianwei Wu, Marco Menarini, Zihe Gao, and Liang Feng. Lithography-free reconfigurable integrated photonic processor. *Nature Photonics*, 17(8):710–716, Aug 2023.

- [45] Changming Wu, Haoqin Deng, Yi-Siou Huang, Heshan Yu, Ichiro Takeuchi, Carlos A. Ríos Ocampo, and Mo Li. Freeform direct-write and rewritable photonic integrated circuits in phase-change thin films. *Science Advances*, 10(1):eadk1361, 2024.
- [46] Tatsuhiro Onodera, Martin M. Stein, Benjamin A. Ash, Mandar M. Sohoni, Melissa Bosch, Ryotatsu Yanagimoto, Marc Jankowski, Timothy P. McKenna, Tianyu Wang, Gennady Shvets, Maxim R. Shcherbakov, Logan G. Wright, and Peter L. McMahon. Scaling on-chip photonic neural processors using arbitrarily programmable wave propagation, 2024.
- [47] Gordon Wetzstein, Aydogan Ozcan, Sylvain Gigan, Shanhui Fan, Dirk Englund, Marin Soljačić, Cornelia Denz, David A. B. Miller, and Demetri Psaltis. Inference in artificial intelligence with deep optics and photonics. *Nature*, 588(7836):39–47, Dec 2020.
- [48] Jianwei Wang, Fabio Sciarrino, Anthony Laing, and Mark G. Thompson. Integrated photonic quantum technologies. *Nature Photonics*, 14(5):273–284, May 2020.
- [49] Emanuele Pelucchi, Giorgos Fagas, Igor Aharonovich, Dirk Englund, Eden Figueroa, Qihuang Gong, Hübel Hannes, Jin Liu, Chao-Yang Lu, Nobuyuki Matsuda, Jian-Wei Pan, Florian Schreck, Fabio Sciarrino, Christine Silberhorn, Jianwei Wang, and Klaus D. Jöns. The potential and global outlook of integrated photonics for quantum technologies. *Nature Reviews Physics*, 4(3):194–208, Mar 2022.

Supplementary Material for “Topological Directional Coupler”

DERIVATION OF THE TWO-EDGE-STATE HAMILTONIAN

The Kane-Mele Hamiltonian can be written as

$$\mathcal{H} = t \sum_{\langle m,n \rangle} a_m^\dagger b_n \sigma_{\alpha\beta}^0 + it_{SOC} \sum_{\langle\langle m,n \rangle\rangle} \nu_{mn} (a_{m\alpha}^\dagger a_{n\beta} + b_{m\alpha}^\dagger b_{n\beta}) \sigma_{\alpha\beta}^z, \quad (\text{S1})$$

where $a_j^\dagger(b_j^\dagger)$ and $a_j(b_j)$ are the creation and annihilation operators for the mode at the A(B)-typed site with index j . $\nu_{mn} = 1$ if the next nearest neighbor (NNN) coupling is clockwise about the lattice center; $\nu_{mn} = -1$ if it is counterclockwise. The spin labels, $\alpha, \beta \in \{\uparrow, \downarrow\}$, and $\sigma_{\alpha\beta}^0, \sigma_{\alpha\beta}^z$ are Pauli matrices acting on the spin subspace. t, t_{SOC} are the nearest neighbor coupling and the NNN spin-orbit coupling, respectively [1].

The corresponding \mathbf{k} -space Hamiltonian in the spin up subspace is

$$H_\uparrow(\mathbf{k}) = \begin{pmatrix} t_{SOC}g(\mathbf{k}) & tf(\mathbf{k}) \\ tf^*(\mathbf{k}) & -t_{SOC}g(\mathbf{k}) \end{pmatrix}, \quad (\text{S2})$$

where $f(\mathbf{k}) = e^{ik_y a_0/\sqrt{3}} + 2 \cos(k_x a_0/2) e^{-i\sqrt{3}k_y a_0/6}$ and $g(\mathbf{k}) = 2[\sin(k_x a_0) - 2 \sin(k_x a_0/2) \cos(\sqrt{3}k_y a_0/2)]$. For convenience, we set $a_0 = 1$ in the following derivation.

In the vicinity of the valleys $\mathbf{K} = (-4\pi/3, 0)$ and $\mathbf{K}' = (4\pi/3, 0)$, Eq. S2 can be expanded with respect to $\delta\mathbf{k} = (\delta k_x, \delta k_y)$ as,

$$H_{\mathbf{K}\uparrow} = v(\delta k_x \sigma_x + \delta k_y \sigma_y) + m\sigma_z \quad \text{and} \quad H_{\mathbf{K}'\uparrow} = v(-\delta k_x \sigma_x + \delta k_y \sigma_y) - m\sigma_z, \quad (\text{S3})$$

where $v = \sqrt{3}t/2$ and $m = 3\sqrt{3}t_{SOC}$.

Eq. S3 can be combined into a form similar to the BHZ Hamiltonian [2],

$$H_\uparrow \equiv \begin{pmatrix} H_{\mathbf{K}\uparrow} & 0 \\ 0 & V^{-1}H_{\mathbf{K}'\uparrow}V \end{pmatrix} = v(\delta k_x \tau_z \otimes \sigma_x + \delta k_y \tau_z \otimes \sigma_y) + m\tau_0 \otimes \sigma_z. \quad (\text{S4})$$

The basis is $(\psi_{\mathbf{K}\uparrow}^R, \psi_{\mathbf{K}\uparrow}^L, \psi_{\mathbf{K}'\uparrow}^R, \psi_{\mathbf{K}'\uparrow}^L)^T$. R (L) represents the RCP (LCP) state. $V = (0, 1; 1, 0)$ is the rotation matrix that exchanges the RCP and LCP bases.

We solve for the edge state Ψ at the interface between two bulks with opposite-signed t_{SOC} [3–5],

$$[-\hat{p}_x \sigma_x + \hat{p}_y \sigma_y + m(y)\sigma_z]\Psi(x, y) = E\Psi(x, y),$$

$$m(y) = \begin{cases} m, & \text{for } y > 0, \\ -m, & \text{for } y < 0, \end{cases} \quad (\text{S5})$$

where $\hat{p}_x = -i\partial/\partial x$, $\hat{p}_y = -i\partial/\partial y$. The dispersion relations of two edge states corresponding to the \mathbf{K} and \mathbf{K}' valleys are linear functions with an identical, positive slope,

$$\omega_{\mathbf{K}\uparrow} = v(k_x + 4\pi/3 + 2\pi N) \quad \text{and} \quad \omega_{\mathbf{K}'\uparrow} = v(k_x - 4\pi/3 + 2\pi N), \quad (\text{S6})$$

where $N \in \mathbb{Z}$, k_x is the wavevector along the interface.

Overall, the entire topological-insulator-based system is reduced to an effective two-state system of the two guided spin-up valley-polarized modes, with which we demonstrate the controllable interference. At the zigzag interface, the two edge states, $\Psi_{\mathbf{K}\uparrow}$ and $\Psi_{\mathbf{K}'\uparrow}$, are well-separated in k -space, so they interact negligibly. On the other hand, at the armchair interface, the two edge states are both folded to be centered at $k_x = 0$ and interact with each other through inter-valley scattering. Consequently, they hybridize into $\Psi_{\pm\uparrow} = (\Psi_{\mathbf{K}\uparrow} \pm \Psi_{\mathbf{K}'\uparrow})/\sqrt{2}$. The two-state Hamiltonians describing the two valley-polarized modes are

$$H_{\text{zigzag}} = \begin{pmatrix} \omega_{\mathbf{K}\uparrow} & 0 \\ 0 & \omega_{\mathbf{K}'\uparrow} \end{pmatrix} \quad \text{and} \quad H_{\text{armchair}} = \begin{pmatrix} \omega_{\mathbf{K}\uparrow} & \Delta/2 \\ \Delta/2 & \omega_{\mathbf{K}'\uparrow} \end{pmatrix}. \quad (\text{S7})$$

DETERMINING TIGHT-BINDING PARAMETERS

We determine the tight-binding parameters by matching the tight-binding and the normalized photonic band structures. Based on table, $|t_{SOC}|/|t| \approx 6.5 \times 10^{-2}$, and $|t_0|/|t| \approx 2.6 \times 10^{-1}$.

TABLE I. calculated tight-binding model parameters

physical quantity	value in photonic band diagram	tight-binding parameter
slope of the ungapped Dirac cone, $\frac{a_0}{2\pi c} \frac{\partial \omega}{\partial k}$	6.6×10^{-2}	$\sqrt{3} t /2$
band gap width of bulk SPC at $\mathbf{K}(\mathbf{K}')$, $\frac{a_0}{2\pi c} \Delta\omega_{\text{SPC}}$	5.2×10^{-2}	$6\sqrt{3} t _{\text{SOC}}$
band gap width of bulk VPC at $\mathbf{K}(\mathbf{K}')$, $\frac{a_0}{2\pi c} \Delta\omega_{\text{VPC}}$	4.0×10^{-2}	$2 t_0 $
splitting between the two spin-up armchair states, Δ_0	see Fig. S1	see Fig. S1

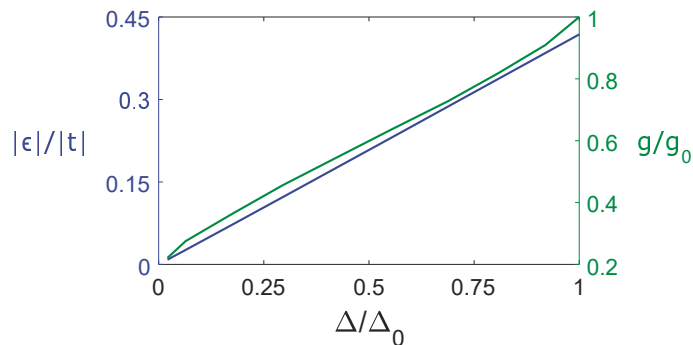


FIG. S1. The relation between the tight-binding model parameter ϵ , the on-site perturbation along the armchair domain wall (left y axis, blue), and the photonic structural parameter g , the height of the gaps most adjacent to the armchair domain (right y axis, green), and the splitting between the two spin-up edge states Δ . When $g = g_0$, the gaps are identical to those in the SPC^{1,2} bulk, and $\Delta = \Delta_0 \approx 1.1 \times 10^{-2} (2\pi c/a_0)$. This splitting corresponds to $|\epsilon| \approx 0.42|t|$ in the tight-binding model and $g = g_0 = 0.15a_0$ in the photonic design.

MICROWAVE EXPERIMENT SETUP

Fig. S2 shows the structure used in the microwave experiment. The dimensions of the SPC^{1,2} and VPC unit cells are the same as in Ref. [5]. The aluminum tripods of VPC are fabricated using wire electrical discharge machining. The tripods between the two parallel plates are supported by two pieces of structural foam (ROHACELL 51HF). We use another piece of structural foam with laser-cut holes to precisely locate the position of every tripod.

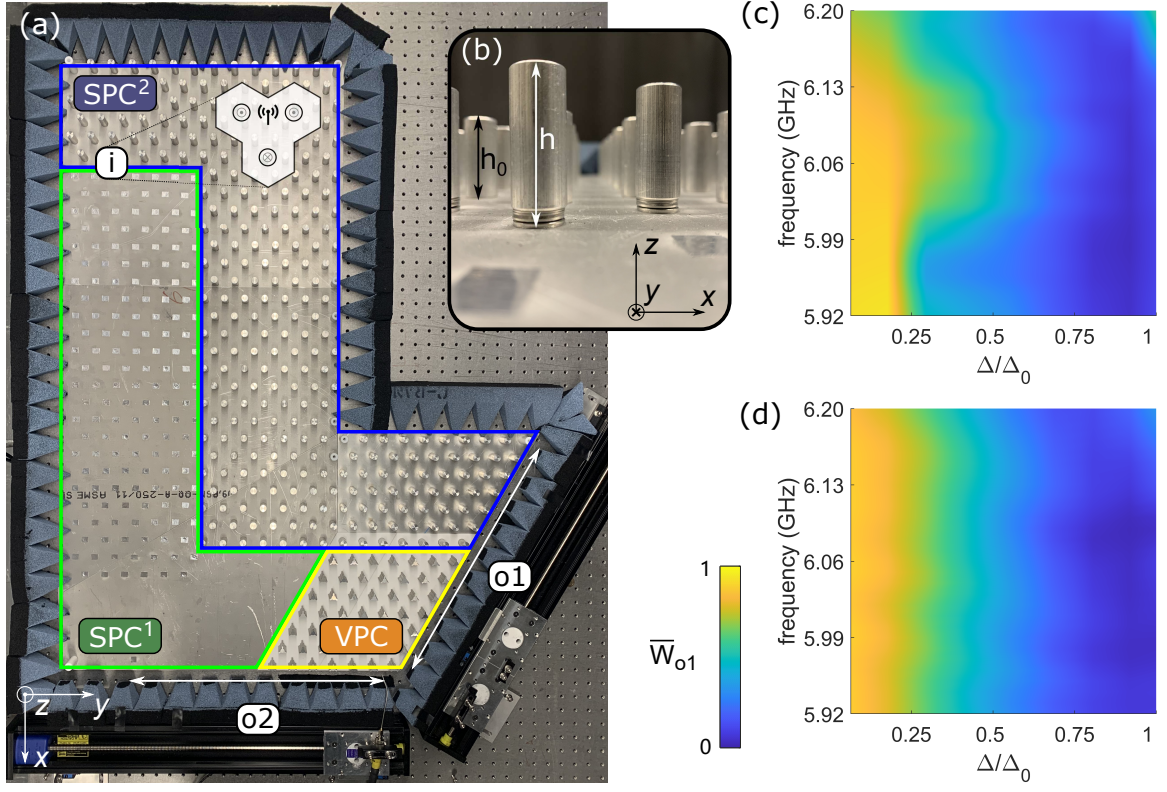


FIG. S2. (a) The microwave experiment setup. We lift the top plate for visualization, so the aluminum rods in the SPC^1 region are not shown. The small squares in the SPC^1 region are pieces of aluminum foil tape used to seal holes on the bottom plate. The entire structure is surrounded by electromagnetic wave absorbers to eliminate the undesired reflection due to the external metallic structure. (b) Perturbed rods along the armchair domain wall. We install aluminum gaskets under the aluminum rods to increase h and decrease g . (c,d) Experiment (c) and COMSOL simulation (d) results of the received energy ratio $\bar{W}_{o1} \equiv W_{o1}/(W_{o1} + W_{o2})$ across the topological band gap for 9 different h configurations.

The source is a 23mm long, \hat{z} -directional antenna made by trimming one lead of a coaxial cable. The source is mounted at the position that ensures the $\Psi_{\mathbf{K}\uparrow}$ state is selectively excited (Fig. S2a inset). The excitation efficiencies of the two valley-polarizations satisfy $\eta_{\mathbf{K}\uparrow}/\eta_{\mathbf{K}'\uparrow} \approx 43$ [5]. (Note that the $\text{SPC}^{1,2}$ regions are flipped compared to those in Ref. [5].) Therefore, the valley \mathbf{K} spin-up state is selectively excited with the setup in Fig. S2.

We use the Keysight N5222A vector network analyzer to perform the measurement. Each set of measurement contains the transmission spectra taken at 257 uniformly spaced positions r_i along the periphery at output o1 or o2 (Fig. S2a). The total amount of the received energy at a output port is calculated by summing $|S_{21}(r_i)|^2$ over all r_i along that port. The detect antenna is mounted on a motor-driven Velmex BiSlide rail. The experiment and simulation results are shown in Fig. S2c,d.

ANALYTICAL CALCULATION

An arbitrary state before entering the armchair domain wall can be written as $\Psi(l=0) = \cos(\theta/2)\Psi_{\mathbf{K}} + e^{i\varphi}\sin(\theta/2)\Psi_{\mathbf{K}'}$, where l is the distance the state traversed along the armchair domain wall. Here the spin-up labels are omitted for clearance. Therefore, state exiting the armchair domain wall of length L is

$$\Psi(l=L) = \left(\cos \frac{\theta}{2} + e^{i\varphi} \sin \frac{\theta}{2} \right) \frac{\Psi_+}{\sqrt{2}} e^{-i\omega_+ \frac{L}{v_g}} + \left(\cos \frac{\theta}{2} - e^{i\varphi} \sin \frac{\theta}{2} \right) \frac{\Psi_-}{\sqrt{2}} e^{-i\omega_- \frac{L}{v_g}}, \quad (\text{S8})$$

where $\omega_{\pm} = \omega_0 \pm \Delta/2$.

Therefore, if the initial state is purely \mathbf{K} -polarized, e.g., $\theta = 0$, the ratio of the $\mathbf{K}(\mathbf{K}')$ -polarization after exiting the

armchair domain wall is,

$$P_{\mathbf{K}} \equiv |\langle \Psi(l = L_{\text{eff}}^{\text{TB}}) | \Psi_{\mathbf{K}} \rangle|^2 = \frac{1}{2} + \frac{1}{2} \cos(L_{\text{eff}}^{\text{TB}} \Delta / v_g);$$

$$P_{\mathbf{K}'} \equiv |\langle \Psi(l = L_{\text{eff}}^{\text{TB}}) | \Psi_{\mathbf{K}'} \rangle|^2 = \frac{1}{2} - \frac{1}{2} \cos(L_{\text{eff}}^{\text{TB}} \Delta / v_g).$$
(S9)

The effective armchair domain wall length $L_{\text{eff}}^{\text{TB}}$ for which the state Ψ experiences the two-edge-state Hamiltonian is shorter than the actual armchair domain wall length, i.e., $L_{\text{eff}}^{\text{TB}} < L$, because Ψ does not turn an abrupt right angle when coupling-in from the zigzag domain wall to the armchair domain wall, or coupling-out from the armchair one to the zigzag one (see Fig. 3c-e in the main text). $L_{\text{eff}}^{\text{TB}} \approx 21.2a_0$ is obtained by fitting $P_{\mathbf{K}}$ to the tight-binding result (Fig. 3b in the main text).

For the photonic structure, first, because the excited state is not ideally \mathbf{K} -polarized, we use $\theta \approx 2 \arccot \sqrt{43}$ to describe the valley-selective source. Moreover, because the photonic structure contains fewer unit cells than the tight-binding model, the finite-size effect in the VPC region becomes notable. Consequently, when Port o1 receives $\Psi_{\mathbf{K}}$, it also receives a small portion of the decay tail of $\Psi_{\mathbf{K}'}$, and vice versa for Port o2 [5]. The energy received by Port o1 and o2 are

$$W_{o1} = |\langle \Psi(l = L_{\text{eff}}^{\text{sim}}) | \Psi_{\mathbf{K}} \rangle|^2 W_{tr} + |\langle \Psi(l = L_{\text{eff}}^{\text{sim}}) | \Psi_{\mathbf{K}'} \rangle|^2 W_{tu};$$

$$W_{o2} = |\langle \Psi(l = L_{\text{eff}}^{\text{sim}}) | \Psi_{\mathbf{K}'} \rangle|^2 W_{tr} + |\langle \Psi(l = L_{\text{eff}}^{\text{sim}}) | \Psi_{\mathbf{K}} \rangle|^2 W_{tu},$$
(S10)

where W_{tr} and W_{tu} are the *transmitted* and *tunneled* energy that we discussed in Ref. [5]. Similar to the tight-binding model, we obtain $L_{\text{eff}}^{\text{sim}}$ by fitting $\overline{W}_{o1} \equiv W_{o1} / (W_{o1} + W_{o2})$ to the COMSOL simulation result. This provides the semi-analytical calculation in Fig. 5b in the main text.

DESIGN THE PERTURBATION IN THE PHOTONIC STRUCTURE

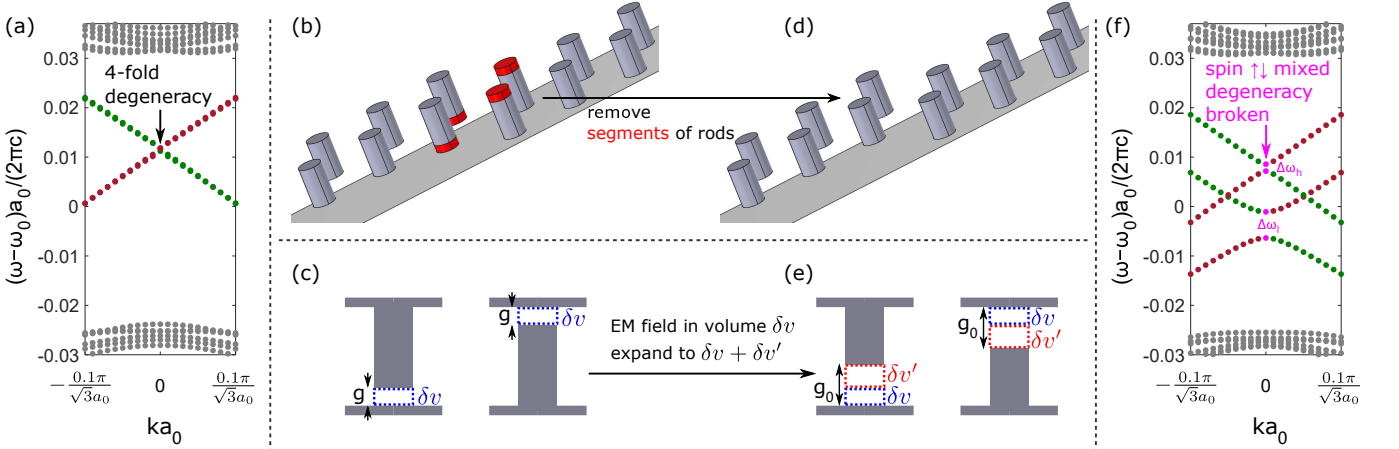


FIG. S3. Band diagrams and the structures of the armchair domain wall with $g = 0.22g_0$ (a,b,c) and $g = g_0$ (d,e,f). The top PEC plate is hidden for better visualization. The schematic diagrams of the structure are not to scale. Increasing g from $0.22g_0$ to g_0 is equivalent to removing the PEC in the shaded red region in (b). This causes the electromagnetic field within volume δv (c, blue dashed line) to expand to volume $\delta v + \delta v'$ (e, blue and red dashed line).

We notice that when $g = 0.22g_0$, the armchair domain wall hosts a 4-fold degeneracy at the Γ point (Fig. S3a-c). This configuration is the starting point for the perturbation-theory-based analysis.

The conventional cavity shape perturbation theory is used to analyze the degeneracy-breaking when a small volume, δv , of perfect electric conductor (PEC) is *added* to the cavity [6, 7]: The electromagnetic field within the volume δv is removed, and the field elsewhere is assumed unchanged. The system Hamiltonian after perturbation is $H = \omega_{p0} I - \Delta$, where ω_{p0} is the degenerate frequency before perturbation. Δ is a matrix depending on the field overlap between different modes within the perturbation volume δv ,

$$\Delta_{ij} = \iiint_{\delta v} (\epsilon_0 \mathbf{E}_i^* \cdot \mathbf{E}_j - \mu_0 \mathbf{H}_i^* \cdot \mathbf{H}_j) dv,$$
(S11)

where i, j are mode indices.

In our structure, however, the degeneracy is broken by removing small pieces of PEC (Fig. S3b,d). Although the conventional cavity shape perturbation theory cannot be directly applied in this scenario, we extend its formalism to model the expansion of the eigenmode field distribution due to the removal of PEC segments. We notice that most of the electromagnetic field is distributed in the gaps between the rod and the top (bottom) plate. Removing segments of the PEC rods is equivalent to expanding those gap volumes from δv to $\delta v + \delta v'$. Therefore, the system Hamiltonian after perturbation becomes $H = \omega_{p0}I + \alpha\Delta$. The minus sign is replaced by a plus sign because the field in the volume δv is not removed but expanded. α is a parameter describing the volume expansion.

While increasing the gap g introduces inter-valley scattering, it also introduces inter-spin coupling in the proximity of the Γ point. The inter-spin coupling is manifested as two avoided crossings centered at $(\omega_h - \omega_0) = 0.009(2\pi c)/a_0$ and $(\omega_l - \omega_0) = -0.007(2\pi c)/a_0$, where the subscripts h and l stand for high- and low-frequency.

Here, we analyze the two avoided crossings using the “extended” cavity perturbation theory. When $g = 0.22g_0$, both the inter-valley and the inter-spin couplings are negligible, and the armchair interface supports a 4-fold degeneracy (Fig. S3a). As the height of the rods most close to the interface decreases, the 4-fold degeneracy is broken (Fig. S3f).

We evaluate the field overlap terms within the gap volume δv (Fig. S3c) and calculate matrix Δ in the spin-valley basis, $\{\Psi_{\mathbf{K}\uparrow}, \Psi_{\mathbf{K}'\uparrow}, \Psi_{\mathbf{K}\downarrow}, \Psi_{\mathbf{K}'\downarrow}\}$. The numerical result shows that all four diagonal entries in Δ are identical, and Δ is in the form of,

$$\bar{\Delta} = \begin{pmatrix} s & p & q & r \\ p & s & r & q \\ q & r & s & p \\ r & q & p & s \end{pmatrix} \approx \begin{pmatrix} 1.00 & -0.57 & -0.06 & 0.03 \\ -0.57 & 1.00 & 0.03 & -0.06 \\ -0.06 & 0.03 & 1.00 & -0.57 \\ 0.03 & -0.06 & -0.57 & 1.00 \end{pmatrix}, \quad (\text{S12})$$

where $\bar{\Delta} \equiv \Delta/\text{diag}(\Delta)$ and $\text{diag}(\Delta) \approx -2.9 \times 10^{-3}(2\pi c)/a_0$. The volume expansion parameter $\alpha \approx 4$.

For convenience, we use four variables s, p, q, r to represent the numerical value of Δ . Eigenfrequencies and eigenmodes of the system after removing segments of rods are in the following table.

eigenfrequencies	eigenmodes
$s + p + q + r$	$(\Psi_{\mathbf{K}\uparrow} + \Psi_{\mathbf{K}'\uparrow} + \Psi_{\mathbf{K}\downarrow} + \Psi_{\mathbf{K}'\downarrow})/2$
$s + p - q - r$	$(\Psi_{\mathbf{K}\uparrow} + \Psi_{\mathbf{K}'\uparrow} - \Psi_{\mathbf{K}\downarrow} - \Psi_{\mathbf{K}'\downarrow})/2$
$s - p + q - r$	$(\Psi_{\mathbf{K}\uparrow} - \Psi_{\mathbf{K}'\uparrow} + \Psi_{\mathbf{K}\downarrow} - \Psi_{\mathbf{K}'\downarrow})/2$
$s - p - q + r$	$(\Psi_{\mathbf{K}\uparrow} - \Psi_{\mathbf{K}'\uparrow} - \Psi_{\mathbf{K}\downarrow} + \Psi_{\mathbf{K}'\downarrow})/2$

The four eigenfrequencies correspond to the two avoided crossings at the Γ point. The higher avoided crossing is centered at $\omega_h = s + p$ with width $\Delta\omega_h = 2(q + r)$; The lower avoided crossing is centered at $\omega_l = s - p$ with width $\Delta\omega_l = 2(q - r)$. The two avoided crossings can hardly be suppressed to a negligible amount simultaneously because that requires $s = p = 0$. With the perturbation of increasing the gap g , $q \approx -2r$ and $\Delta\omega_l \approx 3\Delta\omega_h$ – the higher avoided crossing is suppressed while the lower one is three times as wide, resulting in an increased back-reflection around ω_l (Fig. S4).

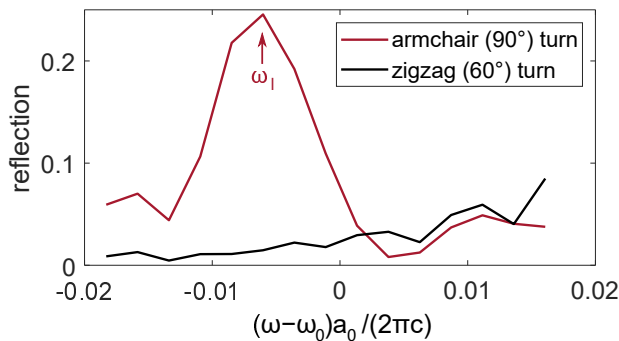


FIG. S4. Frequency-dependent reflection at an armchair (90°) turn. A zigzag (60°) turn is used as a baseline. The reflection increases at ω_l , corresponding to the low-frequency avoided crossing due to inter-spin coupling.

NONZERO REFLECTION AND WEAK TOPOLOGICAL REFLECTION

The avoided crossings at $k = 0$ and the resulting back-reflection indicate that the topological protection of the spin DoF is not strictly robust. In general, the topological protection of photonic systems is weaker than their electronic counterparts: In electronic QSH TIs, the Kramers' degeneracy is protected by the time-reversal symmetry. In photonic QSH TIs, it is the crystalline symmetry and/or the TE/TM polarizations of the electromagnetic wave that help synthesize a pseudo-Kramer's degeneracy. Therefore, there is always an imperfection of the topological protection [8, 9].

An analysis of the SPC^{1,2} reveals the fragile topology [10, 11] in their low-energy bands. When only considering the two bands below the complete band gap, the arguments of the two Wilson loop eigenvalues wind in opposite directions from $-\pi$ to π as functions of the momentum (Fig. S5c). However, when taking all three bands below the band gap into consideration, the nontrivial winding disappears (Fig. S5d).

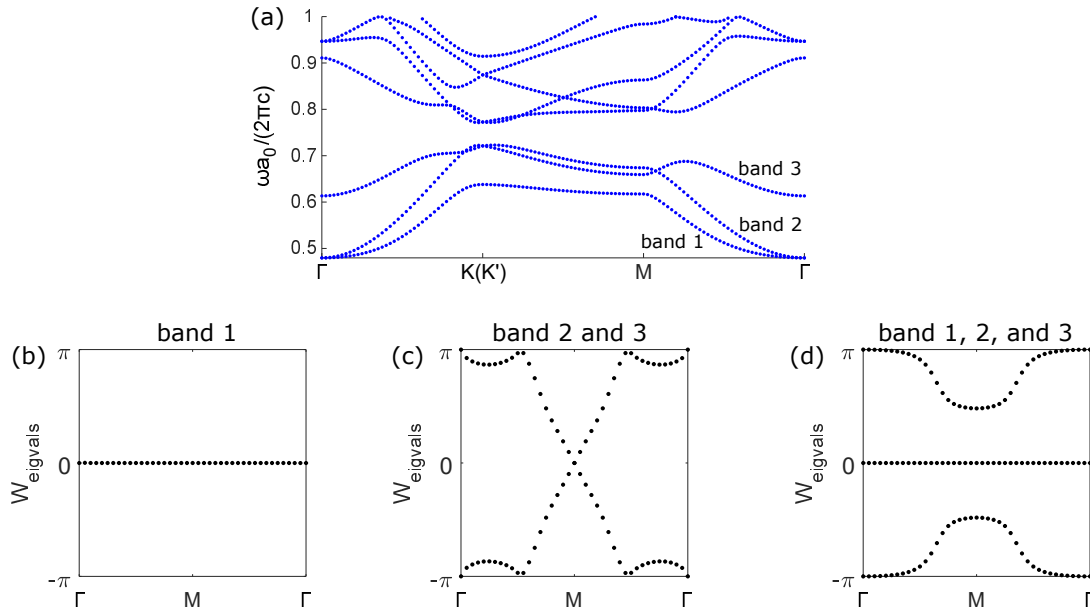


FIG. S5. (a) Photonic band diagram of the SPC^{1,2}. The three bands below the complete band gap are labeled as bands 1, 2, and 3 from low to high frequency. (b-d) The arguments (phases) of the Wilson loop eigenvalues of bands 1, 2, and 3 as functions of the momentum. (b) Only considering the isolated band 1, the Wilson loop eigenvalue has zero phase. (c) Only considering bands 2 and 3, the two Wilson loop eigenvalues wind non-trivially in opposite directions from $-\pi$ to π . (d) Considering all three bands, there is no signature of a non-trivial winding.

The nonzero reflection at the armchair channel at $k = 0$ and the fragile topology suggest that this compact, low-reflection directional coupler does not rely on a strict topological protection. In fact, all lossless waveguides, regardless of their topological classification, can be analyzed using the multi-modal perturbation theory method, and one can design specific interactions in a limited modal subspace by searching over all possible perturbations. Nevertheless, the knowledge of topology and symmetry simplifies the design procedure: We could identify the properties of all four modes based on their topological indices and directly conclude what interfaces cause robust transmission and what create the desired interaction without any computational design algorithms. We also believe that when computational algorithms are deployed to design a photonic structure, the knowledge of the objective-required point group symmetries could accelerate the design procedure by drastically reducing the search space of all possible geometries [12].

REALIZING AN ARBITRARY UNITARY OPERATOR

A general operation in the SU(2) group can be written as [13]

$$\begin{pmatrix} e^{i(\alpha-\beta/2-\delta/2)} \cos \frac{\gamma}{2} & -e^{i(\alpha-\beta/2+\delta/2)} \sin \frac{\gamma}{2} \\ e^{i(\alpha+\beta/2-\delta/2)} \sin \frac{\gamma}{2} & e^{i(\alpha+\beta/2+\delta/2)} \cos \frac{\gamma}{2} \end{pmatrix}. \quad (\text{S13})$$

We demonstrate that this topological interferometer with additional topological waveguides can perform any arbitrary 2×2 unitary operation on the $\Psi_{\mathbf{K}\uparrow}$, $\Psi_{\mathbf{K}'\uparrow}$ states.

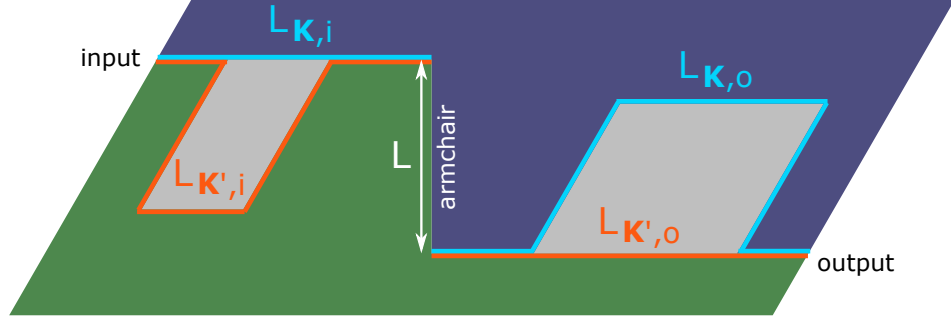


FIG. S6. Schematic of the structure realizing any arbitrary SU(2) operation on the $\Psi_{\mathbf{K}\uparrow}$, $\Psi_{\mathbf{K}'\uparrow}$ states. VPC regions are added to separate the two spin-up states according to their valley indices. Hence, $\Psi_{\mathbf{K}\uparrow}$ and $\Psi_{\mathbf{K}'\uparrow}$ experience different optical paths both before and after interference ($L_{\mathbf{K},i} \neq L_{\mathbf{K}',i}$ and $L_{\mathbf{K},o} \neq L_{\mathbf{K}',o}$).

The evolution operator of the interferometer is

$$e^{-iHL/v_g} = e^{-i\omega_0 L/v_g} \begin{pmatrix} \cos L\Delta/(2v_g) & -i \sin L\Delta/(2v_g) \\ -i \sin L\Delta/(2v_g) & \cos L\Delta/(2v_g) \end{pmatrix}. \quad (\text{S14})$$

With the phase shift accumulated in the zigzag SPC⁺-SPC⁻ waveguides and VPC-SPC waveguides, the overall operation performed by the interferometer-waveguide system can be written as

$$U_{\text{sys}} = e^{-i\omega_0 L/v_g} \begin{pmatrix} e^{i\omega_0 L_{\mathbf{K},o}/v_g} & 0 \\ 0 & e^{i\omega_0 L_{\mathbf{K}',o}/v_g} \end{pmatrix} \begin{pmatrix} \cos L\Delta/(2v_g) & -i \sin L\Delta/(2v_g) \\ -i \sin L\Delta/(2v_g) & \cos L\Delta/(2v_g) \end{pmatrix} \begin{pmatrix} e^{i\omega_0 L_{\mathbf{K},i}/v_g} & 0 \\ 0 & e^{i\omega_0 L_{\mathbf{K}',i}/v_g} \end{pmatrix}, \quad (\text{S15})$$

where $\omega_0 L_{\mathbf{K},o}/v_g$, $\omega_0 L_{\mathbf{K}',o}/v_g$ are the phases accumulated after exiting the interferometer; $\omega_0 L_{\mathbf{K},i}/v_g$, $\omega_0 L_{\mathbf{K}',i}/v_g$ are those before entering the interferometer.

For convenience, we define

$$\phi_0 = \omega_0 \frac{L_{\mathbf{K},i} + L_{\mathbf{K}',o} + L}{v_g} - \frac{\pi}{2}, \quad \phi_1 = \omega_0 \frac{L_{\mathbf{K},o} - L_{\mathbf{K}',o}}{v_g} + \frac{\pi}{2}, \quad \phi_2 = \omega_0 \frac{L_{\mathbf{K}',i} + L_{\mathbf{K},i}}{v_g} + \frac{\pi}{2}. \quad (\text{S16})$$

The extra $\pi/2$ terms are to compensate the imaginary unit i in Eq. S14.

Eq. S15 consequently becomes

$$\begin{aligned} U_{\text{sys}} &= ie^{i\phi_0} \begin{pmatrix} -ie^{i\phi_1} & 0 \\ 0 & 1 \end{pmatrix} \begin{pmatrix} \cos L\Delta/(2v_g) & -i \sin L\Delta/(2v_g) \\ -i \sin L\Delta/(2v_g) & \cos L\Delta/(2v_g) \end{pmatrix} \begin{pmatrix} 1 & 0 \\ 0 & -ie^{i\phi_2} \end{pmatrix} \\ &= \begin{pmatrix} e^{i(\phi_0+\phi_1)} \cos L\Delta/(2v_g) & -e^{i(\phi_0+\phi_1+\phi_2)} \sin L\Delta/(2v_g) \\ e^{i\phi_0} \sin L\Delta/(2v_g) & e^{i(\phi_0+\phi_2)} \cos L\Delta/(2v_g) \end{pmatrix} \end{aligned} \quad (\text{S17})$$

We notice that Eq. S17 can be directly re-written in the form of Eq. S13 by letting

$$L\Delta/v_g = \gamma, \quad \phi_0 = \alpha + \frac{\beta}{2} - \frac{\delta}{2}, \quad \phi_1 = -\beta, \quad \phi_2 = \delta. \quad (\text{S18})$$

SCALING UP THE TDCS AND ANALYZING ENERGY TRANSMISSION EFFICIENCY

To realize a $U(N)$ operation with a Mach-Zehnder interferometer (MZI) grid, properly coupled $N(N-1)/2$ directional couplers are necessary. The first step is to couple two directional couplers with a third one. Here, we provide a schematic of coupling two TDCs with an extra TDC (Fig. S7a). To keep the coupling layout spatially compact, we introduce the design of single-mode ‘‘domain swapper’’ waveguides that use an additional domain of a different VPC to swap domains of different SPCs without altering the transmitted mode (Fig. S7c,d).

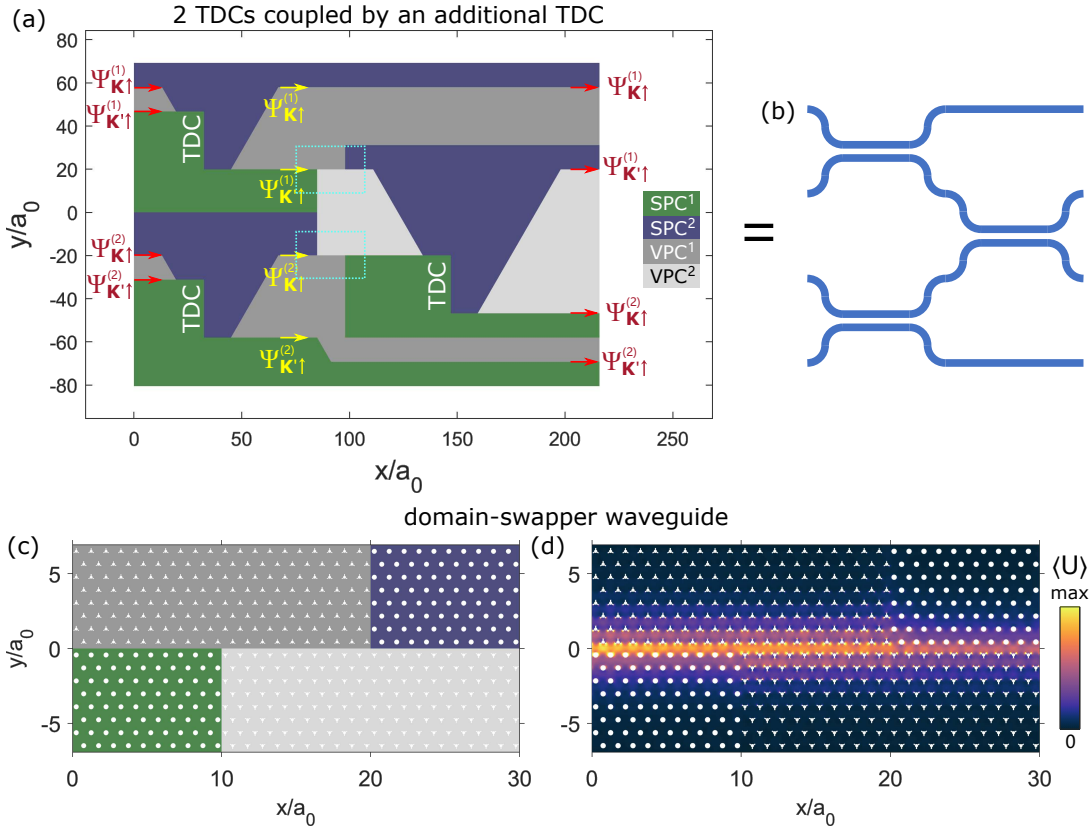


FIG. S7. (a,b) Schematic diagram of two TDCs coupled by an additional TDC. The $\mathbf{K}(\mathbf{K}')$ valley states ($\Psi_{\mathbf{K}(\mathbf{K}')\uparrow}^{(\cdot)}$) at the first and the second TDC are labeled by the superscript. The blue dashed boxes enclose the domain-swapper waveguides. (c,d) The schematic (left) of and the transmitted photonic mode (right) along the single-mode domain-swapper waveguide.

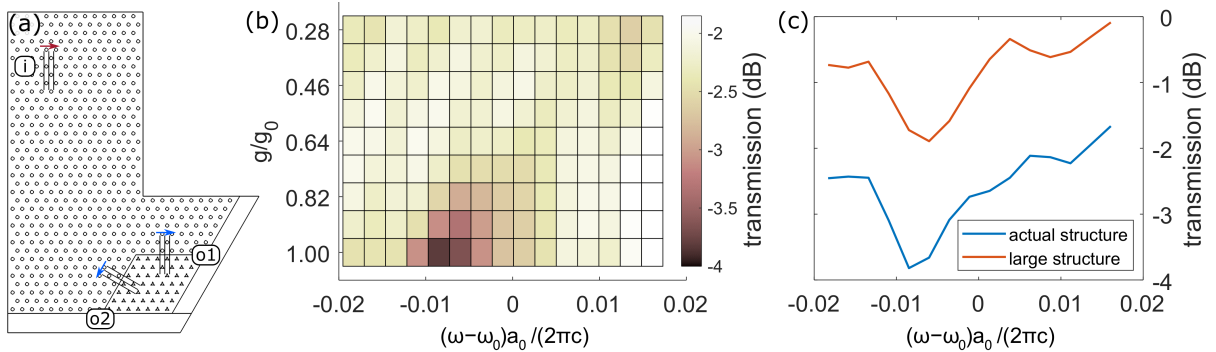


FIG. S8. (a) Schematic of the TDC and the transverse planes for measuring the power flow. (b) Frequency-dependent transmission for nine different configurations. (c) Transmission of the actual structure (the insulating bulk is 7 unit cells deep along the transverse direction, as shown in (a)) and a large structure (the insulating bulk is 14 unit cells deep) when $g/g_0 = 0.91$.

Following Clements et al.'s block implementation [14], each input will travel through an $O(N)$ number of directional couplers, making the received energy reduced to $T^{O(N)}$ of the input, where T is the transmission of one directional coupler. Here, we investigate the transmission of one TDC.

We calculate the perpendicular time-averaged Poynting vector integrated over the transverse intersecting planes (corresponding to output ports o1, o2, and the input port i), $\langle P_{\mathbf{n}}^{port} \rangle \equiv \int_{port} da \langle \mathbf{S} \rangle \cdot \hat{\mathbf{n}}$ (for each port, the result is averaged over three adjacent planes, Fig. S8a), and evaluate the transmission as $T = (\langle P_{\mathbf{n}}^{o1} \rangle + \langle P_{\mathbf{n}}^{o2} \rangle) / \langle P_{\mathbf{n}}^i \rangle$. The frequency-dependent result is presented in Fig. S8b. At high frequencies, $(\omega - \omega_0) a_0 / (2\pi c) \geq 0.002$ (higher than the lower avoided crossing), the transmission is consistently higher than -2.2 dB.

Furthermore, we notice that a majority of the loss is due to the finite-size effect of the structure — the insulating bulk is not large enough to shield all the loss through the exponential tail along the transverse direction. After increasing the depth of the insulating bulk from 7 to 14, we find that the transmission significantly increased. Fig. S8c shows that for the most lossy case ($g/g_0 = 0.91$, when the lower avoid crossing is the widest), doubling the insulating depth increases the transmission by ~ 1.6 dB.

When scaling up multiple TDCs, one also needs to consider how close two TDCs can be placed in parallel without compromising the functionality. When a secondary waveguide is too close to the TDC, optical energy can couple to that secondary waveguide through the evanescent tail. In an SPC waveguide, the propagating mode decays as $e^{-\kappa r_\perp}$ along the transverse direction, where $1/\kappa \approx 2.66a_0$ [5]. Although this decay tail is short, the crosstalk between two parallel waveguides could still be significant if the propagation length is sufficiently long (e.g., 20–30 a_0 for TDCs). To examine the problem, we vary the separation between the primary and a secondary TDC from $8a_0$ to $14a_0$ and measure the energy in the two waveguides after light traverses through the primary TDC. Our finding shows that crosstalk is negligible when the separation exceeds $12a_0$ (Fig. S9).

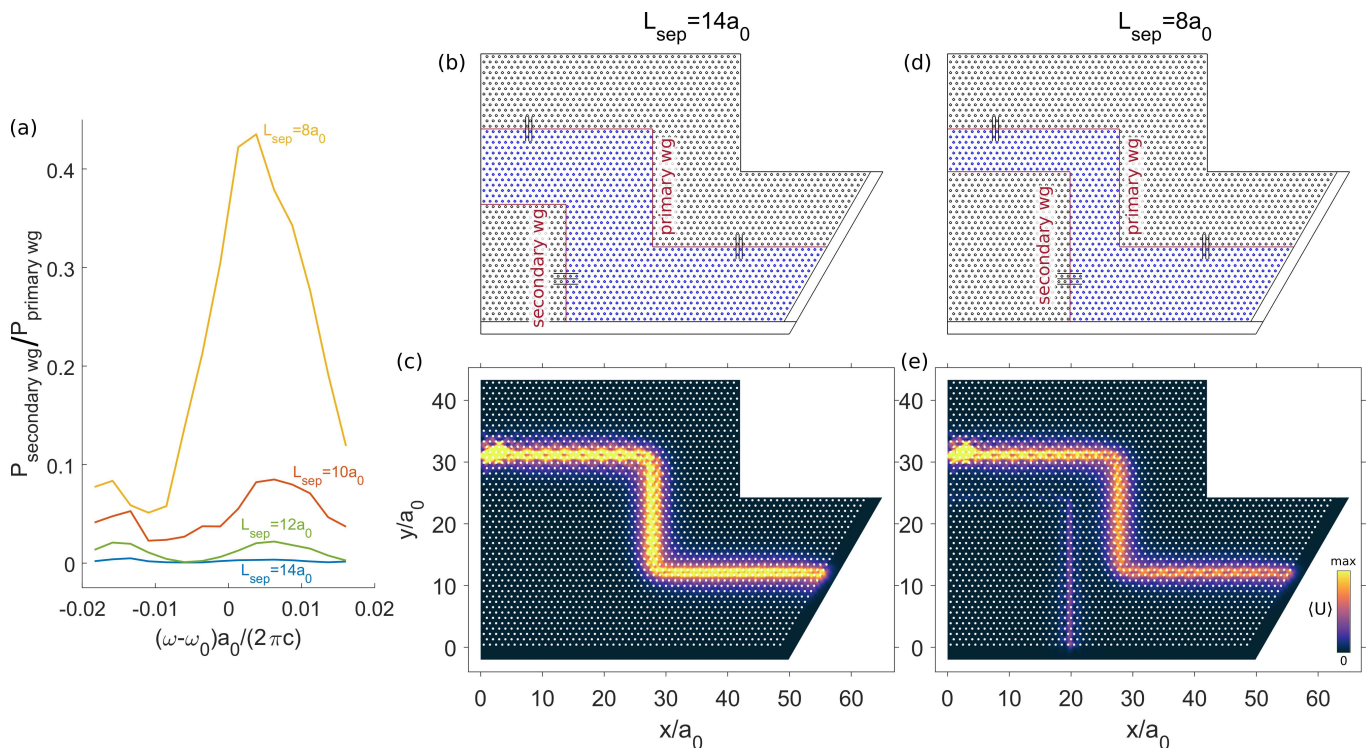


FIG. S9. Crosstalk between the primary and secondary waveguides. (a) The energy flow ratio as a function of the waveguide separation distance. (b,c) The two waveguides are separated by $L_{\text{sep}} = 14a_0$. The coupling from the primary waveguide to the secondary one is negligible. (d,e) $L_{\text{sep}} = 8a_0$. About 30% energy in the primary waveguide couples to the secondary one. The time-averaged energy distributions in (c,e) are at $\omega = \omega_0$, where $\omega_0 \approx 0.75(2\pi c/a_0)$.

FOOTPRINT OF DIRECTIONAL COUPLERS

With the all-dielectric SPCs introduced in the supplementary information of Ref. [15], the SPC-VPC-based TDCs could potentially be realized in the visible or telecom regime. Fig. S10 compares the footprints of TDCs, conventional, and newly emerging directional couplers/beam splitters. TDCs are more compact than conventional directional couplers [16–18], which use transition regions with large radii of curvature to suppress back-reflection. Two unconventional mechanisms, supersymmetric (SUSY) transformation optics and non-Hermitian optics show promise for innovative coupler designs. Compared to SUSY transformation optical mode-converters [19, 20], TDCs are about one order of magnitude shorter because the former requires an adiabatic modification of the refractive index along the propagation direction; Compared to non-Hermitian steering/routing designs [21], TDCs are only marginally smaller. Novel computational design methods, e.g., inverse design, archive the smallest functioning beam-splitting structure [22].

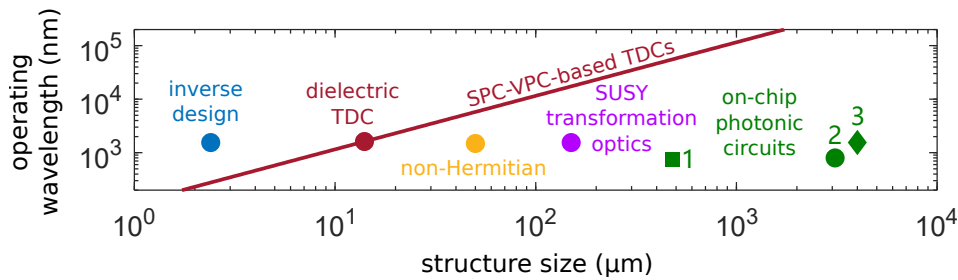


FIG. S10. Comparing the sizes and operating wavelengths of different designs of directional couplers, beam splitters, and routing structures. Red line: the SPC-VPC-based TDCs with different lattice constants. Red dot: the TDC based on the dielectric SPCs introduced in the supplementary material of Ref. [15]. Green dots: designs based on on-chip photonic circuits. 1, 2, and 3 refer to Refs. [16–18], respectively. Magenta dot: the SUSY transformation optical mode converter in Ref. [20]. Yellow dot: the non-Hermitian steering structure in Ref. [21]. Blue dot: the inverse-designed polarization splitter in Ref. [22].

* yl2695@cornell.edu

† gshvets@cornell.edu

- [1] C. L. Kane and E. J. Mele. Quantum spin hall effect in graphene. *Phys. Rev. Lett.*, 95:226801, Nov 2005.
- [2] B. Andrei Bernevig, Taylor L. Hughes, and Shou-Cheng Zhang. Quantum spin hall effect and topological phase transition in hgte quantum wells. *Science*, 314(5806):1757–1761, 2006.
- [3] Frank Schindler. Dirac equation perspective on higher-order topological insulators. *Journal of Applied Physics*, 128(22):221102, 2020.
- [4] János K. Asbóth, László Oroszlány, and András Pályi. *A Short Course on Topological Insulators*. Springer International Publishing, 2016.
- [5] Yandong Li, Yang Yu, Kueifu Lai, Yuchen Han, Fei Gao, Baile Zhang, and Gennady Shvets. Mode-selective single-dipole excitation and controlled routing of guided waves in a multi-mode topological waveguide. *Applied Physics Letters*, 120(22):221702, 2022.
- [6] J. C. Slater. Microwave electronics. *Rev. Mod. Phys.*, 18:441–512, Oct 1946.
- [7] George E. Dombrowski. Matrix formulation of Slater’s cavity perturbation theorem. *Journal of Applied Physics*, 55(7):2648–2650, 04 1984.
- [8] Hai-Xiao Wang, Guang-Yu Guo, and Jian-Hua Jiang. Band topology in classical waves: Wilson-loop approach to topological numbers and fragile topology. *New Journal of Physics*, 21(9):093029, sep 2019.
- [9] Shupeng Xu, Yuhui Wang, and Ritesh Agarwal. Absence of topological protection of the interface states in F_2 photonic crystals. *Phys. Rev. Lett.*, 131:053802, Aug 2023.
- [10] Hoi Chun Po, Haruki Watanabe, and Ashvin Vishwanath. Fragile topology and wannier obstructions. *Phys. Rev. Lett.*, 121:126402, Sep 2018.
- [11] María Blanco de Paz, Maia G. Vergniory, Dario Bercioux, Aitzol García-Etxarri, and Barry Bradlyn. Engineering fragile topology in photonic crystals: Topological quantum chemistry of light. *Phys. Rev. Res.*, 1:032005, Oct 2019.
- [12] Miloslav Capek, Vojtech Neuman, Jonas Tucek, and Lukas Jelinek. Shape regularization and acceleration of topology optimization via point group symmetries. In *2022 16th European Conference on Antennas and Propagation (EuCAP)*, pages 1–4, 2022.
- [13] Michael A. Nielsen and Isaac L. Chuang. *Quantum Computation and Quantum Information*. Cambridge University Press, 2000.
- [14] William R. Clements, Peter C. Humphreys, Benjamin J. Metcalf, W. Steven Kolthammer, and Ian A. Walmsley. Optimal design for universal multiport interferometers. *Optica*, 3(12):1460–1465, Dec 2016.
- [15] Yuhao Kang, Xiang Ni, Xiaojun Cheng, Alexander B. Khanikaev, and Azriel Z. Genack. Pseudo-spin–valley coupled edge states in a photonic topological insulator. *Nature Communications*, 9(1):3029, Aug 2018.
- [16] Mark Dong, Genevieve Clark, Andrew J. Leenheer, Matthew Zimmermann, Daniel Dominguez, Adrian J. Menssen, David Heim, Gerald Gilbert, Dirk Englund, and Matt Eichenfield. High-speed programmable photonic circuits in a cryogenically compatible, visible–near-infrared 200 mm cmos architecture. *Nature Photonics*, 16(1):59–65, Jan 2022.
- [17] Alberto Politi, Martin J. Cryan, John G. Rarity, Siyuan Yu, and Jeremy L. O’Brien. Silica-on-silicon waveguide quantum circuits. *Science*, 320(5876):646–649, 2008.
- [18] Kai-Hong Luo, Sebastian Brauner, Christof Eigner, Polina R. Sharapova, Raimund Ricken, Torsten Meier, Harald Herrmann, and Christine Silberhorn. Nonlinear integrated quantum electro-optic circuits. *Science Advances*, 5(1):eaat1451, 2019.
- [19] Wiktor Walasik, Nitish Chandra, Bikashkali Midya, Liang Feng, and Natalia M. Litchinitser. Mode-sorter design using continuous supersymmetric transformation. *Opt. Express*, 27(16):22429–22438, Aug 2019.

- [20] Jieun Yim, Nitish Chandra, Xilin Feng, Zihe Gao, Shuang Wu, Tianwei Wu, Haoqi Zhao, Natalia M. Litchinitser, and Liang Feng. Broadband continuous supersymmetric transformation: a new paradigm for transformation optics. *eLight*, 2(1):16, Sep 2022.
- [21] Han Zhao, Xingdu Qiao, Tianwei Wu, Bikashkali Midya, Stefano Longhi, and Liang Feng. Non-hermitian topological light steering. *Science*, 365(6458):1163–1166, 2019.
- [22] Bing Shen, Peng Wang, Randy Polson, and Rajesh Menon. An integrated-nanophotonics polarization beamsplitter with $2.4 \times 2.4 \mu\text{m}^2$ footprint. *Nature Photonics*, 9(6):378–382, Jun 2015.